Article

Identifying the intrinsic anti-site defect in manganese-rich NASICON-type cathodes

Yuan Liu[1,2,9], Xiaohui Rong ®[1,2,3,9], Rui Bai[1], Ruijuan Xiao[1], Chunliu Xu[1], Chu Zhang[1], Juping Xu[4,5], Wen Yin[4,5], Qinghua Zhang[1,3], Xinmiao Liang[6], Yaxiang Lu ®[1,7], Junmei Zhao ®[8 ✉], Liquan Chen[1] & Yong-Sheng Hu ®[1,2,3,7 ✉]

Manganese-rich NASICON-type materials have triggered widespread attention for developing advanced polyanionic cathodes, primarily driven by their abundant reserves and promising cycling performance with high operating voltages (~3.8 V for $Mn^{2+/3+/4+}$, versus Na^+/Na). However, the charge/discharge profiles exhibit significant voltage hysteresis, which leads to a limited reversible capacity, thereby preventing their application. Here, we demonstrate that the voltage hysteresis in manganese-rich NASICON-type cathodes ($Na_3MnTi(PO_4)_3$) is closely related to the intrinsic anti-site defect (IASD), which forms during synthesis and is captured in our characterizations. Combining electrochemical analysis and spectroscopic techniques, we draw a comprehensive picture of sluggish Na^+ diffusion behaviours in the IASD-affected structure during cycling, and rationalize the relationship of voltage hysteresis, phase separation and delayed charge compensation. Furthermore, a Mo-doping strategy is developed to decrease the defect concentration, which enhances the initial Coulombic efficiency from 76.2% to 85.9%. Overall, this work sheds light on the voltage hysteresis in NASICON-type cathodes and provides guidelines for designing high-performance polyanionic electrodes.

Electrical energy storage provides a well-established approach for integrating intermittent low-carbon energy sources[1]. Polyanionic-type Na-ion battery cathode materials are expected to meet the expanding demands for large-scale applications, due to their long-term stability, high safety and sustainable reserves, in addition to the abundance and low cost of sodium[2,3]. As a cost-effective choice, manganese-rich NASICON-type cathodes (such as $Na_3MnTi(PO_4)_3$ and $Na_3MnZr(PO_4)_3$) have been proposed[4] and synthesized[5,6] recently, and exhibit a theoretical specific capacity of ~117 mAh g^{-1} with high operating voltages (~3.6 V for $Mn^{2+/3+}$ and ~4.0 V for $Mn^{3+/4+}$ versus Na^+/Na). Unfortunately,

capacity loss and voltage hysteresis seriously deteriorate the reversible capability, and the mechanism of failure remains unclear.

Manganese-rich NASICON-type materials with three-dimensional (3D) Na^+ diffusion channels[7,8] normally exhibit voltage hysteresis in the charge/discharge profiles[6,9,10], which is usually attributed to the low conductivity of polyanionic compounds. Although numerous delicate conductive networks have been designed to diminish the hysteresis, the voltage polarization is still present[11,12]. Recently, Yang et al.[13,14] found that the voltage hysteresis in $Na_3VCr(PO_4)_3$ is caused by the migration of high-valence V^{5+} to the Na1 site (the Wyckoff position is 6b), which

[1]Beijing National Laboratory for Condensed Matter Physics, Institute of Physics, Chinese Academy of Sciences, Beijing, China. [2]College of Materials Science and Optoelectronic Technology, University of Chinese Academy of Sciences, Beijing, China. [3]Yangtze River Delta Physics Research Center Co. Ltd, Liyang, China. [4]Spallation Neutron Source Science Center, Dalang, PR China. [5]Institute of High Energy Physics, Chinese Academy of Sciences, Beijing, PR China. [6]State Key Laboratory of Magnetic Resonance and Atomic and Molecular Physics, Innovation Academy for Precision Measurement Science and Technology, Chinese Academy of Sciences, Wuhan, China. [7]Huairou Division, Institute of Physics, Chinese Academy of Sciences, Beijing, China. [8]CAS Key Laboratory of Green Process and Engineering, State Key Laboratory of Biochemical Engineering, Institute of Process Engineering, Chinese Academy of Sciences, Beijing, China. [9]These authors contributed equally: Yuan Liu, Xiaohui Rong. ✉e-mail: jmzhao@ipe.ac.cn; yshu@iphy.ac.cn
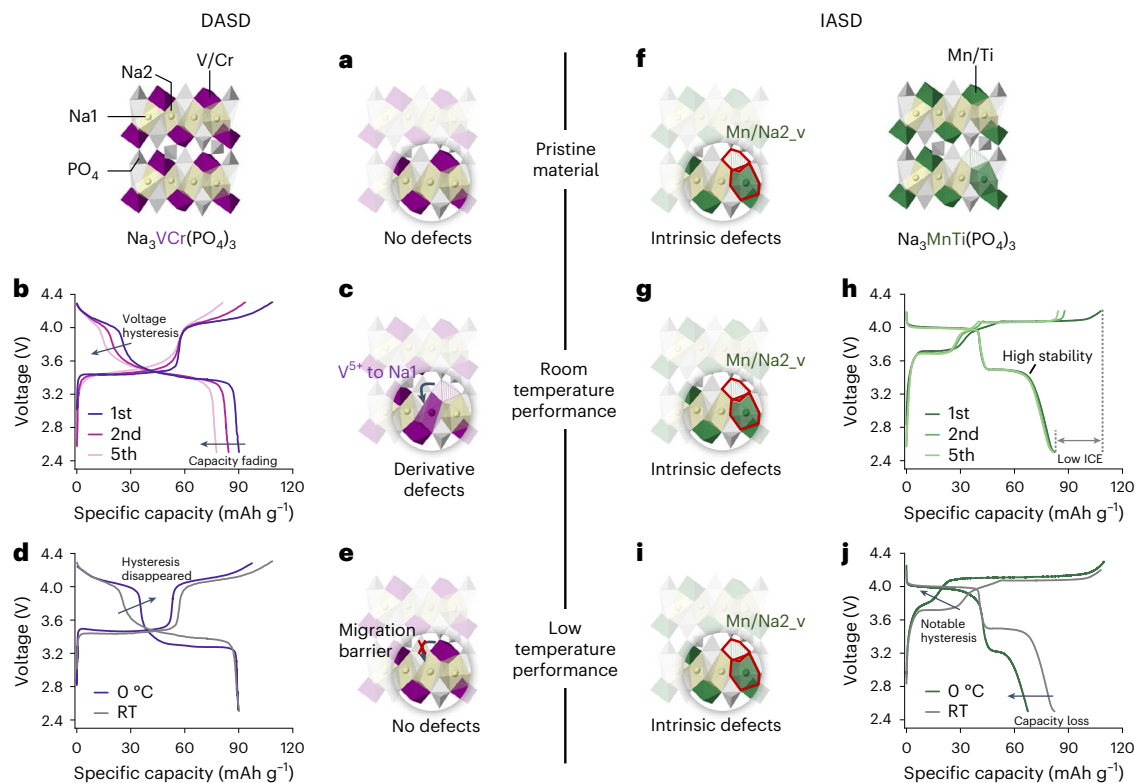
Fig. 1 | The differences between derivative anti-site defect and intrinsic anti-site defect. b,d,h,j, Voltage profiles of $Na_3VCr(PO_4)_3$ (left panels) and $Na_3MnTi(PO_4)_3$ (right panels) at 0.1C (1C = 117 mAh g^{-1}) at room temperature (**b,h**) and 0 °C (**d,j**), respectively. Schematics of the crystal structure are shown on the side. **a,** There are two Wyckoff positions of Na atoms, 6b (denoted by Na1) and 18e (denoted by Na2). The atoms are orderly arranged within the pristine $Na_3VCr(PO_4)_3$. **b–e,** After cycling (**b**), the DASD was generated during desodiation, where V^{5+} migrated to the Na1_vacancy (denoted by V^{5+} to Na1_v) (**c**), and voltage hysteresis was induced. However, a significant migration barrier of V^{5+} (**e**) hinders

the above process at a low temperature, so the voltage hysteresis disappears (**d**). **f–j,** Mn occupation in Na2_vacancy (denoted by Mn/Na2_v) (**f**) during synthesis resulted in the formation of the IASD, and the structure is unchanged in the following cycles (**f,g,i**). RT, room temperature. Therefore, a notable capacity loss is only shown on the initial cycle (**h**), and it is even worse at a low temperature (**j**). Data in **b** and **d** were collected using Digitizer (OriginLab). Panels adapted with permission from: **b**, ref. 14, American Chemical Society; **d**, ref. 13, John Wiley and Sons.

leads to detrimental structural degradation during cycling, and it can be eliminated at low temperatures due to the inhibition of V^{5+} migration. This mechanism was also employed to explain the significant initial capacity loss of $Na_3MnTi(PO_4)_3$ (ref. 15). However, $Na_3MnTi(PO_4)_3$ displays different cycling performance, with significant capacity loss after the initial cycle and outstanding reversibility for the following cycles[11,15]. The above findings imply that different mechanisms (other than that based on the migration of transition metal to alkali sites) might be at play.

Herein we define two types of defects in polyanionic materials to distinguish such different behaviours: derivative anti-site defects (DASDs) generated during the charge/discharge process and intrinsic anti-site defects (IASDs) produced during the synthesis process (Fig. 1a–j). Through spectroscopic, structural and theoretical studies, we reveal that the voltage hysteresis is caused by IASDs of Mn occupation in the Na2 (the Wyckoff position is 18e) vacancy (Mn/Na2_v) in a manganese-rich NASICON-type material ($Na_3MnTi(PO_4)_3$). The Mn/Na2_v IASD blocks Na$^+$ diffusion channels and hampers the redox reaction of Mn$^{2+/3+/4+}$, resulting in voltage polarization and capacity loss. Therefore, we explore a practical strategy to overcome such voltage hysteresis via doping Mo in the transition metal site to increase the formation energy of the IASD so as to lower the defect concentration. As a result, the reversible specific capacity of Mo-doped $Na_3MnTi(PO_4)_3$ increased from 82.1 mAh g^{-1} to 103.7 mAh g^{-1} at 0.1C, and retained 78.7% of the initial capacity after 600 cycles at 0.5C within the voltage range 2.5–4.2 V. These results have implications for

understanding failure mechanisms in a broader range of NASICON-type cathodes and provide an avenue for developing low-cost and high-energy-density batteries.

Capturing the Mn/Na2_v IASD in $Na_3MnTi(PO_4)_3$

Given that the composition of transition metal sites can directly control the reversible capacity of Mn$^{2+/3+/4+}$ redox pairs in $Na_3MnTi(PO_4)_3$ (denoted as NMTP), the element doping strategy (Al^{3+}, Cr^{3+}, Mo^{6+}) was employed to adjust the charge/discharge behaviours (Supplementary Fig. 1) via the sol–gel synthesis method. To our surprise, only 5% Mo doping ($Na_{2.9}MnTi_{0.95}Mo_{0.05}(PO_4)_3$, denoted as NMTP-M) can increase the reversible capacity from 82.1 mAh g^{-1} to 103.7 mAh g^{-1} at 2.5–4.2 V (Supplementary Fig. 2) and eliminate the voltage hysteresis at the same time. First, the structure and morphology of as-prepared NMTP and NMTP-M samples have been characterized to confirm the high quality of the samples. As shown in Supplementary Figs. 3 and 4, the NMTP and NMTP-M are indexed to the rhombohedral $R\bar{3}C$ space group[12,16], and the small amount of Mo in NMTP-M is evenly distributed. Additionally, impurities will occur when the doping amount further increases to 0.1 (Supplementary Figs. 5 and 6). The particles of as-prepared materials are nanosized, ranging from 100 to 500 nm, and coated with amorphous carbon (Supplementary Figs. 7–10). According to the combustion analyser, the carbon content of NMTP and NMTP-M was calculated as 6.43 wt% and 6.77 wt%, respectively, which was also supported by the thermogravimetric (TG) analysis results (Supplementary Fig. 11)[10].
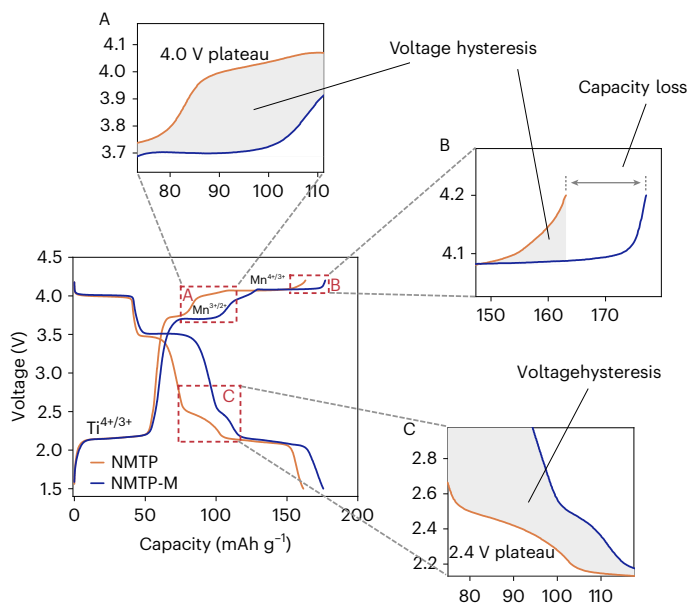
Fig. 2 | Voltage hysteresis and capacity loss of Na₃MnTi(PO₄)₃. Voltage profile of the second galvanostatic cycles of $Na_3MnTi(PO_4)_3$ (NMTP) and $Na_{2.9}MnTi_{0.95}Mo_{0.05}(PO_4)_3$ (NMTP-M) against metallic sodium at a 0.2C rate ($1C = 117$ mAh g^{-1}) within the voltage range 1.5–4.2 V. There are three reversible platforms belonging to Ti$^{4+/3+}$, Mn$^{3+/2+}$ and Mn$^{4+/3+}$. The curves exhibit significant differences, which are highlighted by the red dashed boxes. Insets A–C are magnified views of such zones, where the voltage hysteresis and capacity loss can be clearly observed.

Despite similar phases and morphologies for the two materials, drastically different electrochemical behaviours are shown in the voltage profiles. Notably, these provide the opportunity to accurately capture the location of voltage hysteresis and benefit the interpretation of the failure mechanism afterwards. As illustrated in Fig. 2, the galvanostatic charge/discharge curves of NMTP and NMTP-M vary in the regions shown in A–C. For NMTP, the capacity within the range 3–3.8 V is only 22.3 mAh g^{-1}, and the voltage suddenly rises with a plateau appearing at ~4.0 V (region A), which means a higher charging voltage is needed to fully realize the Mn$^{2+/3+}$ oxidation reaction. Even so, only 1.8 Na$^+$ of NMTP can be extracted at the 4.2 V cutoff, as shown in region B. Similarly, the discharge capacity is only 80.0 mAh g^{-1} at the 2.5 V cutoff, and an additional 2.4 V plateau presents upon further discharge (region C). In contrast, the voltage polarization and capacity loss are alleviated in NMTP-M. Furthermore, the two plateaus in regions A and C are widely present in manganese-rich NASICON-type cathodes and can be defined as characteristic curves of voltage hysteresis[6,9].

To reveal the failure mechanism, the atomically resolved crystal structure was characterized. High-angle annular dark-field (HAADF) images of the as-prepared materials were collected to directly identify the structural differences at atomic resolution. Figure 3a,b shows HAADF-scanning transmission electron microscopy (STEM) images of NMTP and NMTP-M along the [2̄21] direction, respectively, and the corresponding structure models are shown in Supplementary Fig. 12. HAADF images were obtained using the Z-contrast imaging technique; thus, the bright spots correspond to the Mn/Ti atomic columns in the octahedral 12c sites, and the grey spots correspond to Na sites. There are two crystallographic Na sites, denoted as Na1 and Na2 (ref. 17); however, the grey spots of Na sites are easily disturbed by noise signals. To address this issue, grayscale statistics at Na sites were conducted. The grey-level histograms of Na1 (Fig. 3c) and Na2+P (Fig. 3d) sites were collected in normalized HADDF-STEM images (Fig. 3a,b), where the higher brightness and wider distribution of Na2+P sites in NMTP

indicate that transition metal ions are located in the Na2 atomic columns. Furthermore, the Gaussian fitting based on least-squares minimization has been used to reveal the atomic columns information due to the noise following a normal distribution[18–20]. As shown in Supplementary Fig. 13a,b, the IASD-affected Na2+P atomic columns with a higher Z-contrast can be directly captured in the NMTP sample (details in Supplementary Note 1).

Then, ab initio density functional theory (DFT) calculations were implemented to reveal the type of transition metal ions occupying the Na vacancies. The crystal structure of NMTP is built on the 3D matrix of angle-sharing [MnO₆]/[TiO₆] octahedra and [PO₄] tetrahedra. There are 18 Na$^+$ ions for 24 sites; thus, incompletely occupied Na1 and Na2 sites provide vacancies for disordered transition metal ions. All configurations in the primary cell (Mn/Na1_v, Mn/Na2_v, Ti/Na1_v, Ti/Na2_v) were taken into consideration to rationalize the anti-site defect model[21], and the formation energies of IASD are collected in Fig. 3e. Schematic diagrams of the lowest energy structure corresponding to every IASD species are displayed in the figure. It can be found that the O sites are distorted after the Ti occupies the Na site, and the Ti/Na_v shows higher formation energy (1.00, 0.85 eV/primary cell for Ti/Na1_v and Ti/Na2_v, respectively). Therefore, the transition metal in Na2_v can be attributed to Mn. As was captured in HADDF-STEM images, the formation energy of the Mn/Na2_V IASD is the lowest, which is 0.61 eV. Meanwhile, the mechanism of the Mo-doping strategy can also be revealed by DFT calculations. The unit cell was expanded threefold to approximate the low Mo-doping amount, and then the defect-free and Mn/Na2_v IASD structures of the Mo-doped materials were established (Supplementary Fig. 14a,b). Excitingly, the formation energy of the Mn/Na2_v IASD rises to 0.96 eV after Mo doping, which is 57.4% higher than that of the undoped sample. This finding reveals that the concentration of IASDs can be directly controlled by adjusting formation energies, and rationalizes the Mo-doping strategy. Furthermore, the Rietveld refinement profiles of neutron powder diffraction (NPD) patterns were performed to quantify the concentration of Mn/Na2_v IASD (Fig. 3f,g, Supplementary Fig. 15 and Supplementary Tables 1–3). As shown in Fig. 3f and Supplementary Table 1, the site occupancy factor of Mn/Na2_v IASD in pristine NMTP is as high as 4.99%. In contrast, the concentration drops precipitously to 0.51% in the NMTP-M, benefiting from the higher defect formation energy of the Mo-doped structure (Fig. 3g and Supplementary Table 2). On the basis of the above finding, we provide solid evidence of the Mn/Na2_v IASD in the NMTP pristine material.

Structural evolution and charge compensation during cycling

Previous studies indicated that the migration channel around the Na2 site is the rate-determining step, with a higher diffusion barrier in the NASICON-type structure[22,23]. Accordingly, the Mn/Na2_v IASD will directly increase the Na$^+$ diffusion barrier due to the blocked pathway, and inhibit the intercalation and de-intercalation processes. As mentioned in Fig. 2, significant voltage hysteresis can be captured in regions A (4.0 V charging voltage) and C (2.4 V discharging voltage). Thus, it is essential to depict the whole picture of structural evolution and charge compensation in these two plateaus, and clarify the role of Mn/Na2_v IASD in voltage hysteresis.

Operando X-ray diffraction, ex situ X-ray absorption spectroscopy (XAS) and galvanostatic intermittent titration technique (GITT) characterization were used to reveal the structural evolution and charge compensation. As shown in Fig. 4a, different phase transition behaviours of the NMTP and NMTP-M are illustrated by the operando X-ray diffraction patterns. The reflection peaks of the (003) plane during the charging process are ~35.4°, ~36.6° and ~37.7°, corresponding to Na₃, Na₂ and Na₁ phases, respectively (Supplementary Figs. 16 and 17)[24]. For NMTP, the Na₃ and Na₂ phases coexist in the 4.0 V charging plateau, and the Na₃ phase disappears slowly until the voltage rises to 4.05 V, which means
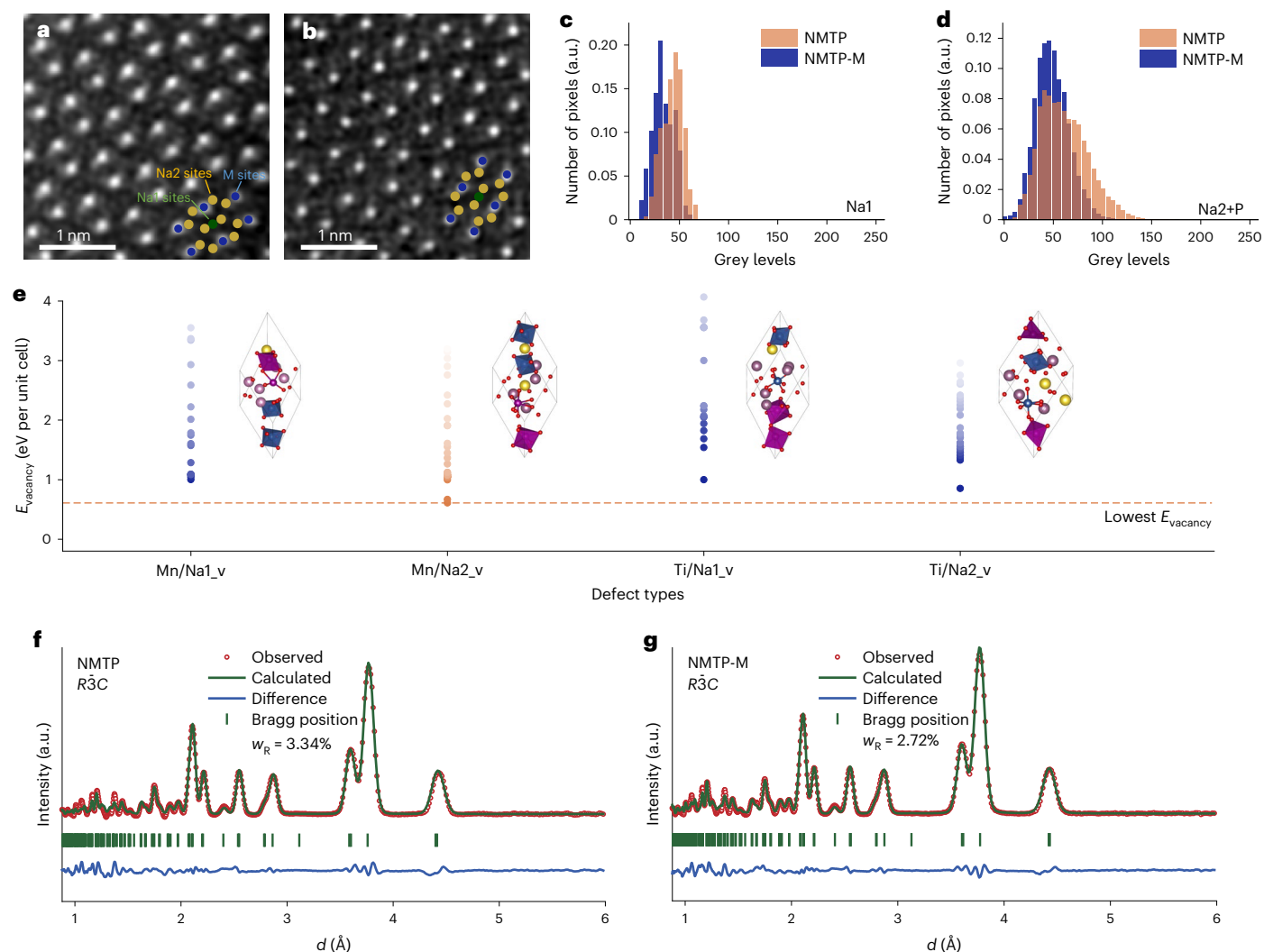
Fig. 3 | Structural characterizations of as-synthesized materials.
a,b, Atomic-resolution HADDF-STEM images of $Na_3MnTi(PO_4)_3$ (**a**) and
$Na_{2.9}MnTi_{0.95}Mo_{0.05}(PO_4)_3$ (**b**) along the [2$\bar{2}\bar{1}$] zone axis. The labelling of atomic
sites is shown in the lower right inset; the orange circles are the Na2+P sites, the
Na1 sites are green and the M sites are blue. **c,d**, Grey-level histograms of Na1 (**c**)
and Na2+P (**d**) sites were collected in **a** and **b**. The grey-level histograms were
used to suppress noise interference of the light Na atoms. **e**, The formation
energies of anti-site defects (Mn/Na1_v, Mn/Na2_v, Ti/Na1_v, Ti/Na2_v). Schematic

illustrations of crystal structures corresponding to the lowest formation energy
are shown to the right. Na1 is yellow, Na2 is light purple, O is red, Mn is purple and
Ti is blue. **f,g**, Refinement profile of neutron diffraction and refined structure of
$Na_3MnTi(PO_4)_3$ (**f**) and $Na_{2.9}MnTi_{0.95}Mo_{0.05}(PO_4)_3$ (**g**). In the profiles, the red hollow
circle and green solid curves represent the observed and calculated intensities,
respectively. The solid blue lines at the bottom indicate residual curves. The
upper and lower green ticks indicate the peak positions of $Na_3MnTi(PO_4)_3$.

a delayed $Na_3 \rightarrow Na_2$ reaction occurs during charging. Similarly, the
insertion reaction of the Na_2 phase to the Na_3 phase in NMTP cannot be
fully completed at the 2.5 V cutoff voltage. As a result, the (003) peak of
NMTP at 2.5 V is 35.5°, higher than the 35.4° of pristine material, which
indicates the extracted Na sites are not fully embedded (Fig. 4b). Until
discharge to 2.2 V, the $Na_2 \rightarrow Na_3$ reaction of NMTP can be achieved with
the (003) peak shifted back to the pristine position. In sharp contrast,
the NMTP-M shows a smooth phase transition behaviour without the
separation of the $Na_3 \rightarrow Na_2$ reaction. Based on the above finding, we
can find that the $Na_3 \rightarrow Na_2$ reaction of NMTP separates into the two
step processes of $Na_3 \rightarrow Na_2$ and delayed $Na_3 \rightarrow Na_2$ reaction, and phase
separation occurs (Supplementary Figs. 18 and 19). Therefore, we
can speculate that a sluggish Na^+ diffusion pathway around the IASD
leads the $Na_2 \leftrightarrow Na_3$ reaction in the IASD-affected domain out of the
thermodynamic equilibrium potential. Of course, evidence of phase
transition in NMTP and NMTP-M is not enough; the thermodynamic
equilibrium potential and redox pairs in the voltage hysteresis plateau
should also be confirmed.

The thermodynamic equilibrium potential can be measured
using the GITT characterization technique. GITT measurements were
conducted after the third cycle of 0.1C cycling (versus Na^+/Na) with a
titration step at 0.1C of 15 min and a relaxation step of 2 h. As shown
in Fig. 4c, the GITT profiles of NMTP illustrate that the open-circuit
voltage of the additional 4.0 V plateaus back to 3.63 V after fully relaxing
(corresponding to the $Mn^{2+/3+}$ oxidation reaction). It turned out that
the thermodynamic equilibrium potential of the delayed $Na_3 \rightarrow Na_2$
reaction is unchanged. Figure 4d shows the overpotential of
as-prepared materials, and the polarization voltage of NMTP is as
high as 0.33 V during charging. Meanwhile, the overpotential of NMTP
is higher than NMTP-M during the whole $Mn^{2+/3+/4+}$ redox process and
shows voltage hysteresis. On the basis of the above findings, we
deduce that the voltage hysteresis is caused by the high diffusion barrier
around the IASD-affected domains. Furthermore, the calculated
Na^+ diffusion coefficients share a similar phenomenon, in which the
diffusion coefficient of NMTP-M during the $Mn^{2+/3+/4+}$ redox reaction
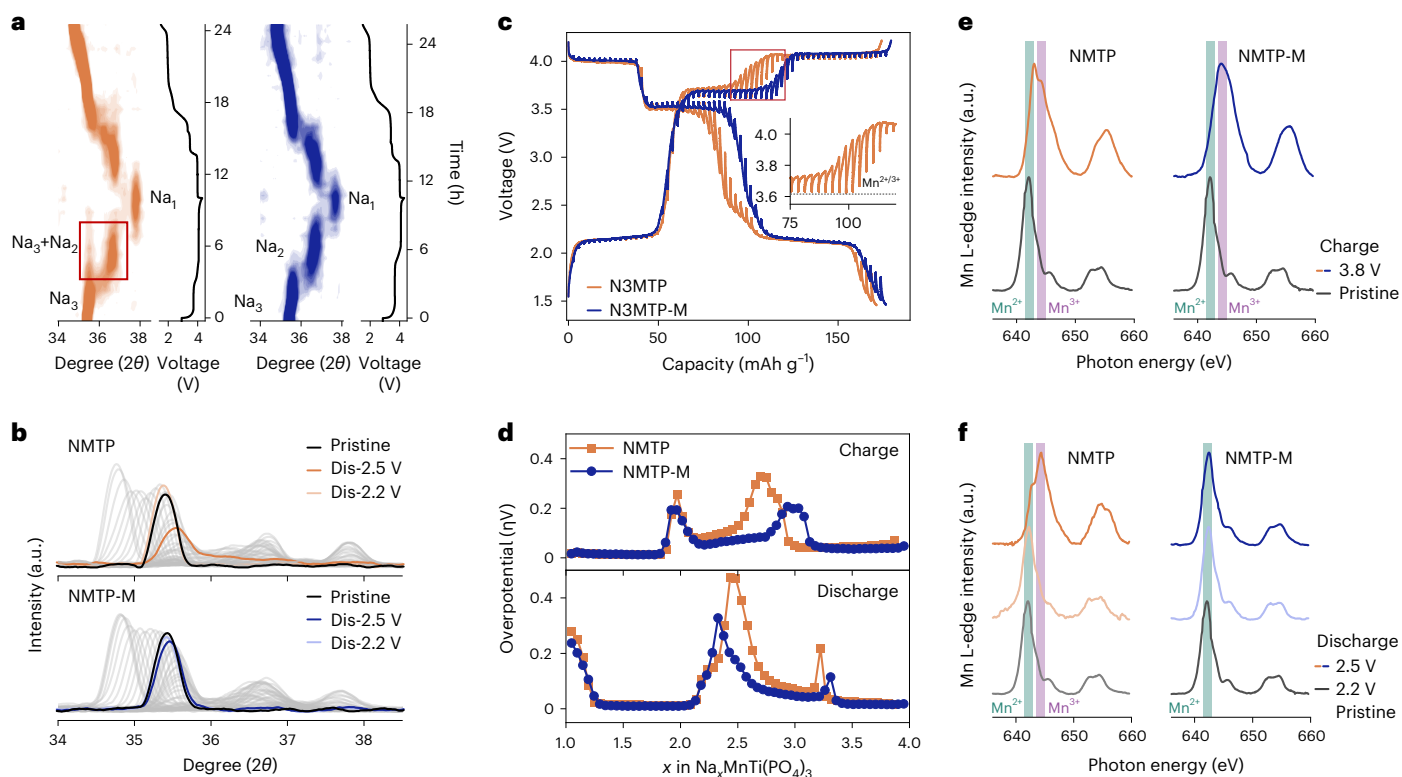has been significantly improved (Supplementary Figs. 20 and 21).

Fig. 4 | Operando and ex situ characterizations of structural evolution and charge compensation. a,b, Operando X-ray diffraction spectra during the first cycles at 0.1C between 1.5 and 4.3 V. Two-dimensional contour plots (**a**) highlighting the evolution of the (003) Bragg diffraction peak, and the phase separation (marked with red box). Na_1, Na_2 and Na_3 represent the $Na_xMnTi(PO_4)_3$ ($x = 1, 2, 3$) phases, respectively. The stacked curves (**b**) were prepared to intuitively exhibit the shift of the (003) diffraction peaks. The black, light yellow (light blue) and yellow (blue) curves correspond to the initial (pristine),

2.5 V discharged (Dis-2.5 V) and 2.2 V discharged (Dis-2.2 V) NMTP (NMTP-M), respectively. **c,d,** GITT profiles (**c**) and overpotentials (determined by GITT) (**d**) of materials. The polarization voltage was defined as the difference between the 2 s standing and relaxation for 2 h. **e,f,** Soft XAS of the Mn L edge for materials in **c** pristine, charge 3.8 V (**e**) and in **d** pristine, discharge 2.5 V and discharge 2.2 V (**f**) of the first cycle collected in total electron yield mode. The data for the yellow curves were collected from NMTP, and blue from NMTP-M.

To determine the charge compensation processes of the as-prepared materials, the total electron yield mode of ex situ soft XAS was obtained. The Mn L edge XAS spectra of the two materials were collected in pristine, 3.8 V charged, 2.5 V discharged and 2.2 V discharged states (Fig. 4e,f)[25,26]. As shown in Fig. 4e, NMTP and NMTP-M have an Mn^{2+} initial state that is also supported by Mn K edge XAS (Supplementary Figs. 22 and 23). Note that the absorption spectra differ at 3.8 V charged. NMTP clearly shows a low-energy peak (~642.9 eV) belonging to Mn^{2+} at the left of the Mn^{3+} absorption peak (~644.0 eV). However, a single absorption peak (~644.0 eV) dominated by Mn^{3+} presents in NMTP-M. This result reveals that the oxidation reaction of the $Mn^{2+/3+}$ redox pair in the NMTP structure cannot be fully carried out at the 3.8 V cutoff (Supplementary Fig. 24). Similarly, the Mn L edge XAS spectra at 2.5 V and 2.2 V discharged states demonstrate that the charge compensation of Mn^{3+} in the NMTP structure is inadequate at the 2.5 V cutoff (Fig. 4f), which is consistently confirmed by the Mn K edge XAS (Supplementary Fig. 22a,b). Finally, X-ray photoelectron spectroscopy (XPS) spectra results demonstrate that Mo in NMTP-M is hexavalent during cycling (Supplementary Fig. 25)[27]. As a result, in agreement with the findings of operando X-ray diffraction and GITT, the charge compensation result also demonstrates that the voltage hysteresis behaviour during charge/discharge is caused by a sluggish kinetic process around the Mn/Na2_v IASD rather than a different thermodynamic process.

In the voltage hysteresis plateau of NMTP (such as the additional 4.0 V plateau), the evolution of phase ($Na_3{\rightarrow}Na_2$) and valence ($Mn^{2+}{\rightarrow}Mn^{3+}$), even the thermodynamic equilibrium potential, coincides with that of the material without IASD. Therefore, we can deduce

that the voltage hysteresis is caused by the inhibited kinetic process around IASD-affected domains. On the basis of the above finding, we summarize the phase transition and charge compensation processes of NMTP with colour-coded squares, and provide a comprehensive picture in Fig. 5 to illustrate the origin of voltage hysteresis affected by the Mn/Na2_v IASD. The $x = 3$ of $Na_xMnTi(PO_4)_3$ is defined as the initial state (Na_3 phase), and the IASD-affected domains are marked by red squares. When the charging voltage rises to 3.8 V, the unaffected domain is transformed from the Na_3 phase to the Na_2 phase. However, the IASD-affected domain maintains the Na_3 phase due to the Na^+ diffusion barrier. Therefore, the Na_2 and Na_3 phases coexist in the additional 4.0 V plateau during further charging, and the XAS results reveal a delayed $Mn^{2+/3+}$ reaction. Then, delayed $Mn^{2+/3+}{\rightarrow}Mn^{3+/4+}{\rightarrow}$delayed $Mn^{3+/4+}$ takes place in a sequence. As mentioned in Fig. 2 (region B), the delayed $Mn^{3+/4+}$ cannot be fully achieved at 4.2 V cutoff, and only 1.8 Na^+ can be extracted. So, the capacity corresponding to the delayed $Mn^{3+/4+}$ reaction is less than for the delayed $Mn^{2+/3+}$ reaction. It should be noted that the discharging reactions are not symmetrically distributed. As shown in Supplementary Fig. 26a–c, the capacity corresponding to the delayed $Mn^{3+/4+}$ reaction disappears when the NMTP cathode cycles within the voltage range 2.5–4.2 V, which means the delayed $Mn^{3+/4+}$ reaction is achieved under the additional 2.4 V plateau during discharge. Therefore, the reactions during discharge are $Mn^{3+/4+}{\rightarrow}Mn^{2+/3+}{\rightarrow}$delayed $Mn^{2+/3+/4+}$.

Furthermore, we reveal the insertion/extraction behaviours of the subsequent cycles in the IASD-affected domain. Supplementary Fig. 26a,c shows charging voltage profiles of the first five cycles of
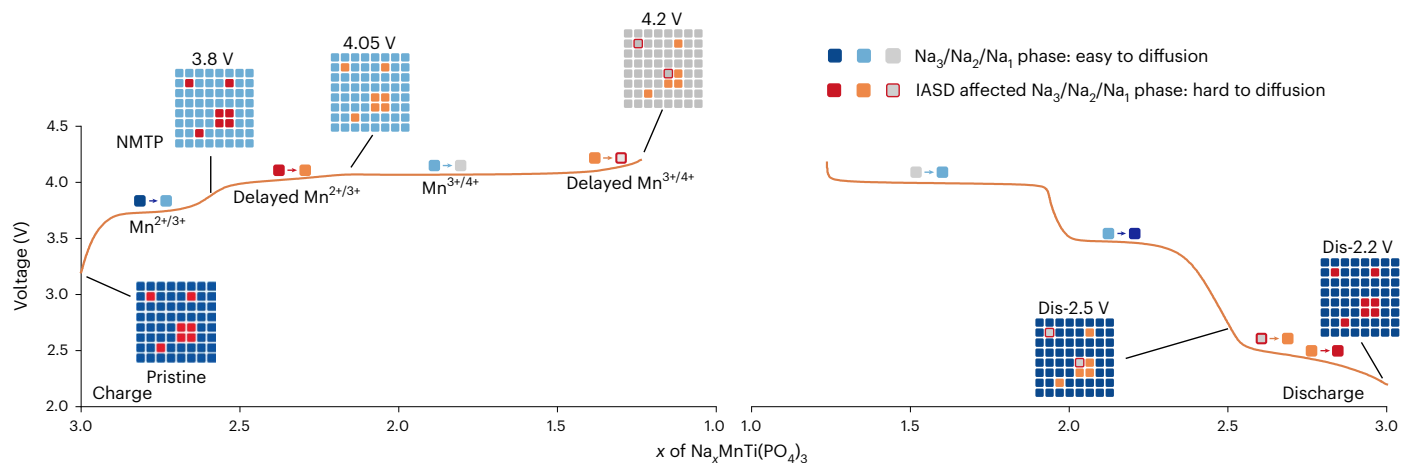
Fig. 5 | Effect of IASD on Na$^+$ de-intercalation. Illustrations of Na$^+$ de-intercalation behaviours demonstrate the relationship between the diffusion barrier and electrochemical performance. The yellow curves are the voltage profile of the first galvanostatic cycle of NMTP, which is against metallic sodium at a 0.2C rate (1C = 117 mAh g^{-1}) within the voltage range 1.5–4.2 V. The charge curve is shown on the left, the discharge curve is shown on the right, and the structure evolution illustrations (pristine, 3.8 V charge, 4.05 V charge, 4.2 V charge, 2.5 V discharge (Dis-2.5 V), 1.5 V discharge (Dis-1.5 V)) are shown on the side. The blue, light blue and light grey squares represent the domains without IASD belonging to Na$_3$, Na$_2$ and Na$_1$ phases, respectively; the red, orange and light grey squares with red boxes represent the IASD-affected domains belonging to Na$_3$, Na$_2$ and Na$_1$ phases, respectively.
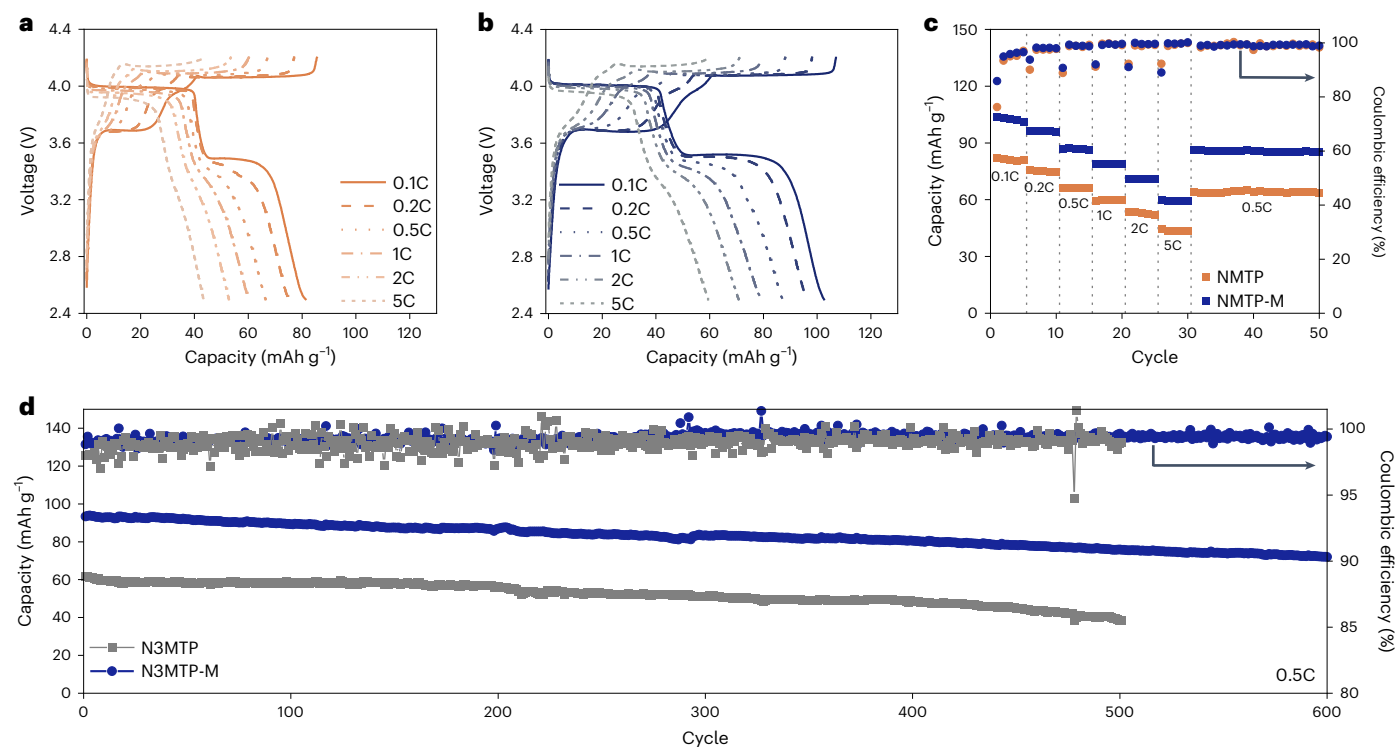

Fig. 6 | Superior electrochemical performance of NMTP-M over NMTP. a,b, Charge/discharge profile of NMTP (**a**) and NMTP-M (**b**) at 0.1C, 0.2C, 0.5C, 1C, 2C and 5C within a voltage range of 2.5–4.2 V. **c,** Rate capability of the materials. **d,** Cycling performance of the materials at a current rate of 0.5C at a cutoff potential of 4.3 V. Here, 1C is defined as 117 mA g^{-1}.

NMTP between 2.5 and 4.2 V. It can be found that the capacity of the delayed Mn$^{2+/3+/4+}$ reaction in NMTP significantly decreases, and exhibits a limited reversible capacity with good cycle stability. Here, the capacity loss and the diminishing voltage hysteresis of the following cycles indicate that the Na$^+$ sites in the IASD-affected domains are not embedded at 2.5 V cutoff. More importantly, the overlapping charging curve of two to five cycles demonstrates that the IASDs in the NMTP structure are unchanged, and no more IASDs are generated during cycling. The schematics for these findings are illustrated in Supplementary Fig. 26d.

Electrochemical performance

To evaluate the excellent electrochemical performance of the Mo-doping materials, we constructed half-cells with NMTP and NMTP-M as cathodes, and all tests were performed at room temperature. The voltage profiles of NMTP and NMTP-M at different current rates (0.1C, 0.2C, 0.5C, 1C, 2C and 5C, where 1C is defined as 117 mAh g^{-1}) are shown in Fig. 6a,b, respectively. Surprisingly, NMTP-M exhibits a reversible capacity of 103.7 mAh g^{-1} at 0.1C, which is much higher than that of NMTP (82.1 mAh g^{-1}). Figure 6c shows that the Mo-doped

materials have higher specific capacities at different current rates. Furthermore, NMTP-M can be cycled stably for up to 600 cycles at 0.5C, while maintaining a high Coulombic efficiency of ~99.9% (Fig. 6d and Supplementary Figs. 27–29). The outstanding results demonstrate that Mn/Na2_v IASD is the dominant factor limiting the electrochemical performance, and Mo doping is a simple and effective method for improving performance. Interestingly, Mo-doped NMTP-M with an Mn content of 1.2 was synthesized in this work, and its pure phase was confirmed by the X-ray diffraction pattern (Supplementary Fig. 30). It should be noted that the Mo-doping method is equally valid and delivers a high reversible capacity of 111.4 mAh g^{-1} (Supplementary Fig. 31).

A full-cell with NMTP-M cathode, hard carbon (HC) anode and 1 M NaPF$_6$ in ethylene carbonate/diethyl carbonate (EC/DEC) (1:1) as the electrolyte was demonstrated. The performance of the HC anode was investigated in a half-cell first, as shown in Supplementary Fig. 32, which delivers a specific capacity of 324 mAh g^{-1} at 0.1C. The charge/discharge curve of the NMTP-M‖HC full-cell is illustrated in Supplementary Fig. 33a, which presents a high reversible capacity of 89.3 mAh g^{-1} at 0.5C. Moreover, the full-cell still retained good cycling stability even at a high cutoff voltage of 4.2 V (Supplementary Fig. 33b).

Conclusions

On the basis of the aforementioned experimental results, we clearly defined and classified DASD and IASD in polyanionic compounds. The IASD in pristine material is caused by the low defect formation energy, and the low diffusion barrier of transition metal to alkali sites leads to the generation of the DASD during cycling. This finding rationalizes the significant voltage hysteresis and capacity loss of NMTP. We demonstrate that the voltage hysteresis of NMTP is closely related to the formation of the Mn/Na2_v IASD. As a result, a sluggish Na$^+$ de-intercalation behaviour with significant voltage polarization was captured, which is the cause of the phase separation and incomplete valence evolution. To tackle these issues, we developed a Mo-doping strategy, which markedly increased the formation energy of Mn/Na2_v IASD in the Na$_3$MnTi(PO$_4$)$_3$ structure, thereby decreasing the defect concentration and improving the reversible capacity from 82.1 mAh g^{-1} to 103.7 mAh g^{-1}.

In addition, we believe the Mn/Na2_v IASD is also present in the majority of the manganese-rich NASICON-type cathodes (for example, Na$_4$MnAl(PO$_4$)$_3$ (ref. 9), Na$_3$MnZr(PO$_4$)$_3$ (ref. 6), etc.) because they share very similar structures and voltage profiles with NMTP. Moreover, characteristic curves of voltage hysteresis (as mentioned in Fig. 2) were also observed in these compounds. In a broad sense, this work provides guidelines for designing high-performance manganese-rich NASICON-type cathodes, and delivers in-depth views of defects in polyanionic materials.

Methods

Synthesis

The sol–gel method was used to prepare Na$_3$MnTi(PO$_4$)$_3$ and Na$_{2.9}$MnTi$_{0.95}$Mo$_{0.05}$(PO$_4$)$_3$ samples. Stoichiometric amounts of NaCH$_3$COO (99.0%, Alfa), Mn(CH$_3$COO)$_2$ (98.0%, Alfa), Ti(OCH(CH$_3$)$_2$)$_4$ (97.0%, Alfa) and critic acid (99.5%, Alfa) were dissolved in ethanol to form the pre-NMTP gel. Then, the aqueous solutions of NH$_4$H$_2$PO$_4$ (99.5%, Sigma-Aldrich) and (NH$_4$)$_6$Mo$_7$O$_{24}$ (99.0%, Sigma-Aldrich) were added to ethanol, followed by stirring, evaporation and drying at 85 °C. Finally, the precursor powder was heated for 10 h at 650 °C under an argon atmosphere.

Electrochemical characterization

As-synthesized materials were mixed with conductive additive (Super P) and binder (PVDF, Solef5130, Solvay) (80:10:10 ratios) in N-methylpyrrolidone (NMP, Tci) to prepare composite cathodes. The obtained slurry was coated onto the aluminium foil, predried in a drying/heating chamber with forced convection at 55 °C for 4 h and thoroughly dried in the vacuum drying oven at 120 °C for 6 h.

Then, the coated foil was punched into discs with a diameter of 10 mm (~3.0 mg cm^{-2}). The sodium ingot (99.8%, Alfa) was rolled into sodium foil, and cut into a diameter of 12 mm. The glass fibre filter paper (Whatman, GF/D) served as the separator. A 1.0 M NaClO$_4$ (98%, Alfa) solution in propylene carbonate (PC, Sigma-Aldrich) containing 2 vol% 4-fluoro-1,3-dioxolan-2-one (FEC, Hairong) was used as the electrolyte. For the Na$_3$MnTi(PO$_4$)$_3$ and Na$_{2.9}$MnTi$_{0.95}$Mo$_{0.05}$(PO$_4$)$_3$ half-cells, the 2032 coin-type cells were fabricated in an Ar atmosphere glovebox. The full-cell was fabricated with Na$_{2.9}$MnTi$_{0.95}$Mo$_{0.05}$(PO$_4$)$_3$ cathode, HC as the anode and 1.0 M NaPF$_6$ in EC/DEC (Hairong) as the electrolyte. All electrochemical tests were carried out using a LAND CT3200A battery cycler (LANHE SYSTEM). GITT measurements were then conducted after the three precycles at 0.1C between 1.5 and 4.3 V (versus Na$^+$/Na) with a titration step at 0.1C of 15 min and a relaxation step of 2 h.

To prepare ex situ samples for characterization, the cathode was charged/discharged with Swagelok-type cells. A self-standing cathode film was fabricated by the rolling method with as-prepared materials, conductive additive (Super P) and polytetrafluoroethylene as the binder (80:10:10 ratio). The anode, electrolyte and separator were consistent with the coin-type half-cell. After cycling, ex situ samples were extracted in an Ar atmosphere glovebox. Subsequently, dimethyl carbonate (DMC, Sigma-Aldrich) was used to wash samples.

Combustion analyser

The combustion analyser (CS844 carbon/sulfur determinator) was used to obtain the accurate carbon content. A preweighed sample was combusted in a stream of purified oxygen. As the temperature increased, the carbon present in the sample was oxidized to carbon dioxide (CO$_2$) and carbon monoxide (CO). The gas flow continued past a heated catalyst, where CO was converted to CO$_2$. Finally, the amount of CO$_2$ was accurately determined using a flow meter and infrared spectroscopy.

Diffraction measurements

X-ray diffraction data were collected using a Bruker D8 Advance diffractometer (CuKα radiation source, λ Kα1 = 1.54056 Å, λ Kα2 = 1.54439 Å). Operando X-ray diffraction measurements were performed using an airtight electrochemical cell, and the carbon-coated aluminium foil served as the window. The neutron data were characterized at the China Spallation Neutron Source (Multiple Physics Instrument). As-prepared pristine sample (~2 g) was measured for 6 h under ambient conditions. Furthermore, GSAS2 was performed to calculate the Rietveld refinement profile of the neutron data.

Electron microscopy

The morphology of the cathode particle was observed by scanning electron microscopy (S-4800, Hitachi) with acceleration voltages of 10 kV. The transmission electron microscope (JEOL ARM-200F) was used to capture the atomic-resolution STEM image (operated at 200 keV), and electrons from 90–370 mrad were collected for the HAADF-STEM images. The Fourier filter was used to minimize the effect of contrast noise.

X-ray photoemission spectroscopy

XAS measurements were conducted at beamline BL11W and BL02B02 at the Shanghai Synchrotron Radiation Facility. XAS tests were carried out in transmission mode with a Si(111) double-crystal monochromator, and analysed using the ATHENA software package.

Solid-state nuclear magnetic resonance

^{23}Na MAS NMR was measured on a Bruker AVANCE III 400 MHz NMR spectrometer (9.4 T) with a 3.2 mm commercial probe using a one-pulse programme with a pulse of 1.4 μs. The spin rate was 15 kHz. The ^{23}Na chemical shifts were referenced to a 1 mol l^{-1} solution of NaCl(aq) at 0 ppm.

Raman spectroscopy

The Raman measurements were performed at room temperature using a HORIBA LabRAM HR Evolution Raman spectrometer with a 532 nm excitation wavelength between 200 and 1,600 cm^{-1}.

DFT calculations

Spin-polarized DFT calculations were performed using the Vienna ab initio simulation package code[28–30] using the generalized gradient approximation of Perdew–Burke–Ernzerhof[31]. The rotationally invariant Dudarev method[32] (DFT+U) was used to correct the self-interaction error of conventional DFT for correlated d electrons. A cutoff energy of 520 eV was used for all calculations. The force exerted on each atom was ensured to be less than 0.01 eV Å^{-1} for structural relaxation. The Brillouin zone was sampled by a 3 × 3 × 3 and 2 × 2 × 1 Γ-centred k-mesh for the rhombohedral and hexagonal models, respectively. We used enumlib to enumerate possible orderings[33] and selected 20 configurations with the lowest electrostatic energy as candidate structures, further stimulated by the DFT structural relaxation and static energy calculations. In this way, the configurations with high energies, which have little possibility of existing in the real material, were eliminated. The ab initio molecular dynamics simulations of the rhombohedral phase have been carried out for the no-anti-site model, the anti-site-Mn model and the no-anti-site Mo-doped model at 900 K.

Data availability

The data supporting the findings of this study are available within the article and its Supplementary Information files. Source data are provided with this paper.

References

1. Dunn, B., Kamath, H. & Tarascon, J. M. Electrical energy storage for the grid: a battery of choices. *Science* **334**, 928–935 (2011).
2. Rudola, A., Sayers, R., Wright, C. J. & Barker, J. Opportunities for moderate-range electric vehicles using sustainable sodium-ion batteries. *Nat. Energy* **8**, 215–218 (2023).
3. Jin, T. et al. Polyanion-type cathode materials for sodium-ion batteries. *Chem. Soc. Rev.* **49**, 2342–2377 (2020).
4. Pan, H., Hu, Y.-S. & Chen, L. Room-temperature stationary sodium-ion batteries for large-scale electric energy storage. *Energy Environ. Sci.* **6**, 2338–2360 (2013).
5. Gao, H., Li, Y., Park, K. & Goodenough, J. B. Sodium extraction from NASICON-structured Na$_3$MnTi(PO$_4$)$_3$ through Mn(III)/Mn(II) and Mn(IV)/Mn(III) redox couples. *Chem. Mater.* **28**, 6553–6559 (2016).
6. Gao, H. et al. Na$_3$MnZr(PO$_4$)$_3$: a high-voltage cathode for sodium batteries. *J. Am. Chem. Soc.* **140**, 18192–18199 (2018).
7. Goodenough, J. B., Hong, H. Y. P. & Kafalas, J. A. Fast Na$^+$-ion transport in skeleton structures. *Mater. Res. Bull.* **11**, 203–220 (1976).
8. Deng, Z. et al. Fundamental investigations on the sodium-ion transport properties of mixed polyanion solid-state battery electrolytes. *Nat. Commun.* **13**, 4470 (2022).
9. Wang, Q. et al. Experimental and theoretical investigation of Na$_4$MnAl(PO$_4$)$_3$ cathode material for sodium-ion batteries. *Chem. Eng. J.* **425**, 130680 (2021).
10. Zhu, T. et al. Dual carbon decorated Na$_3$MnTi(PO$_4$)$_3$: a high-energy-density cathode material for sodium-ion batteries. *Nano Energy* **70**, 104548 (2020).
11. Sun, X. et al. Dual carbon decorated Na$_3$MnTi(PO$_4$)$_3$ as an advanced cathode for sodium-ion batteries. *Ionics* **26**, 3919–3927 (2020).
12. Zhu, T. et al. Realizing three-electron redox reactions in NASICON-structured Na$_3$MnTi(PO$_4$)$_3$ for sodium-ion batteries. *Adv. Energy Mater.* **9**, 2338–2360 (2019).
13. Liu, R. et al. Counter-intuitive structural instability aroused by transition metal migration in polyanionic sodium ion host. *Adv. Energy Mater.* **11**, 2003256 (2020).
14. Liu, R. et al. Exploring highly reversible 1.5-electron reactions (V^{3+}/V^{4+}/V^{5+}) in Na$_3$VCr(PO$_4$)$_3$ cathode for sodium-ion batteries. *ACS Appl. Mater. Interfaces* **9**, 43632–43639 (2017).
15. Zhang, J., Lin, C., Xia, Q., Wang, C. & Zhao, X. S. Improved performance of Na$_3$MnTi(PO$_4$)$_3$ using a non-stoichiometric synthesis strategy. *ACS Energy Lett.* **6**, 2081–2089 (2021).
16. Gao, H. & Goodenough, J. B. An aqueous symmetric sodium-ion battery with NASICON-structured Na$_3$MnTi(PO$_4$)$_3$. *Angew. Chem. Int. Ed. Engl.* **55**, 12768–12772 (2016).
17. Jian, Z. et al. Atomic structure and kinetics of NASICON Na$_x$V$_2$(PO$_4$)$_3$ cathode for sodium-ion batteries. *Adv. Funct. Mater.* **24**, 4265–4272 (2014).
18. De Backer, A., Martinez, G. T., Rosenauer, A. & Van Aert, S. Atom counting in HAADF STEM using a statistical model-based approach: methodology, possibilities, and inherent limitations. *Ultramicroscopy* **134**, 23–33 (2013).
19. Lee, K. et al. STEM image analysis based on deep learning: identification of vacancy defects and polymorphs of MoS$_2$. *Nano Lett.* **22**, 4677–4685 (2022).
20. Lin, R., Zhang, R., Wang, C., Yang, X. Q. & Xin, H. L. TEMImageNet training library and AtomSegNet deep-learning models for high-precision atom segmentation, localization, denoising, and deblurring of atomic-resolution images. *Sci. Rep.* **11**, 5386 (2021).
21. Chung, S. Y., Choi, S. Y., Lee, S. & Ikuhara, Y. Distinct configurations of antisite defects in ordered metal phosphates: comparison between LiMnPO$_4$ and LiFePO$_4$. *Phys. Rev. Lett.* **108**, 195501 (2012).
22. Zhang, Z. et al. Correlated migration invokes higher Na$^+$-ion conductivity in NaSICON-type solid electrolytes. *Adv. Energy Mater.* **9**, 1902373 (2019).
23. Zou, Z. et al. Relationships between Na$^+$ distribution, concerted migration, and diffusion properties in rhombohedral NASICON. *Adv. Energy Mater.* **10**, 2001486 (2020).
24. Park, S. et al. Crystal structure of Na$_2$V$_2$(PO$_4$)$_3$, an intriguing phase spotted in the Na$_3$V$_2$(PO$_4$)$_3$–Na$_1$V$_2$(PO$_4$)$_3$ system. *Chem. Mater.* **34**, 451–462 (2021).
25. Zhuo, Z., Hu, J., Duan, Y., Yang, W. & Pan, F. Transition metal redox and Mn disproportional reaction in LiMn$_{0.5}$Fe$_{0.5}$PO$_4$ electrodes cycled with aqueous electrolyte. *Appl. Phys. Lett.* **109**, 023901 (2016).
26. Qiao, R. et al. Direct evidence of gradient Mn(II) evolution at charged states in LiNi$_{0.5}$Mn$_{1.5}$O$_4$ electrodes with capacity fading. *J. Power Sources* **273**, 1120–1126 (2015).
27. Gruenert, W. et al. Analysis of molybdenum(3d) XPS spectra of supported molybdenum catalysts: an alternative approach. *J. Phys. Chem.* **95**, 1323–1328 (2002).
28. Kresse, G. & Furthmüller, J. Efficiency of ab-initio total energy calculations for metals and semiconductors using a plane-wave basis set. *Comput. Mater. Sci.* **6**, 15–50 (1996).
29. Kresse, G. & Furthmuller, J. Efficient iterative schemes for ab initio total-energy calculations using a plane-wave basis set. *Phys. Rev. B* **54**, 11169–11186 (1996).
30. Shi, S. et al. Multi-scale computation methods: their applications in lithium-ion battery research and development. *Chin. Phys. B* **25**, 018212 (2016).
31. Perdew, J. P., Burke, K. & Ernzerhof, M. Generalized gradient approximation made simple. *Phys. Rev. Lett.* **77**, 3865–3868 (1996).
32. Dudarev, S. L., Botton, G. A., Savrasov, S. Y., Humphreys, C. J. & Sutton, A. P. Electron-energy-loss spectra and the structural stability of nickel oxide: an LSDA+U study. *Phys. Rev. B* **57**, 1505–1509 (1998).
33. Hart, G. L. W., Nelson, L. J. & Forcade, R. W. Generating derivative structures at a fixed concentration. *Comput. Mater. Sci.* **59**, 101–107 (2012).

Author contributions

Y.-S.H. and J.Z. designed and supervised the project. Y.L. synthesized, characterized (X-ray diffraction, XAS, TG, SEM, NPD, Raman) and electrochemically tested the samples and analysed the data with X.R. and R.B. X.L. performed the NMR measurements and analysis. Q.Z. performed the STEM measurements and analysis. J.X. and W.Y. performed neutron diffraction measurements and analysis. R.X. designed and performed DFT calculations and analysis. C.Z. performed the TEM and electron energy loss spectroscopy measurements and analysis. Y.L., X.R., and Y.-S.H. wrote the manuscript. All the authors participated in the discussion to improve the paper and made revisions of the whole manuscript.

Competing interests

The authors declare no competing interests.

Additional information

Supplementary information The online version contains supplementary material available at https://doi.org/10.1038/s41560-023-01301-z.

Correspondence and requests for materials should be addressed to Junmei Zhao or Yong-Sheng Hu.

Peer review information *Nature Energy* thanks Zdeněk Sofer, Yan Wang and the other, anonymous, reviewer(s) for their contribution to the peer review of this work.

Reprints and permissions information is available at www.nature.com/reprints.